Asmita Korde-Patel, Richard K. Barry, Tinoosh Mohsenin, "Application of compressive sensing for gravitational microlensing events," J. Astron. Telesc. Instrum. Syst. 8(1) 018002 (18 February 2022) https://doi.org/10.1117/1.JATIS.8.1.018002

Application of compressive sensing for gravitational microlensing events

Asmita Korde-Patel,[a,b,*] Richard K. Barry,[a] and Tinoosh Mohsenin[b]
[a]NASA Goddard Space Flight Center, Greenbelt, Maryland, United States
[b]University of Maryland, Baltimore County, Baltimore, Maryland, United States

Abstract. Compressive sensing (CS) is a unique mathematical technique for simultaneous data acquisition and compression. This technique is particularly apt for time-series photometric measurements; we apply CS to time-series photometric measurements specifically obtained due to gravitational microlensing events. We show the error sensitivity in detecting microlensing event parameters through simulation modeling. Particularly, we show the relation of both the amount of error and its impact on the microlensing parameters of interest. We derive statistical error bounds to apply those as a baseline for analyzing the effectiveness of CS application. Our results of single and binary microlensing events conclude that we can obtain error less than 1% over a three-pixel radius of the center of the microlensing star by using 25% Nyquist rate measurements. © *2022 Society of Photo-Optical Instrumentation Engineers (SPIE)* [DOI: 10.1117/1.JATIS.8.1.018002]

Keywords: compressive sensing; gravitational microlensing; data acquisition and compression.

Paper 21048 received Apr. 26, 2021; accepted for publication Jan. 28, 2022; published online Feb. 18, 2022.

1 Introduction

Compressive sensing (CS) is a simultaneous data acquisition and compression technique, where data compression is performed at the detector front-end itself. CS is a mathematical theory that allows sampling at a sub-Nyquist rate by exploiting sparsity in data sets. In this work, we assess the application of CS to gravitational microlensing events. Our work is primarily applicable for space-flight instruments, which exhibit tremendous limitations for onboard space flight resources as well as data transmission bandwidth.

Gravitational microlensing is an astronomical phenomenon during which a massive body, such as a star or a black hole, or a system of bodies, may pass in front of a distant source star causing the deflection of light from the source, effectively briefly magnifying and brightening that source. Using this technique exoplanets can be detected. The phenomenology of microlensing requires the exceedingly precise alignment of a source star and an intervening massive body.[1,2] Consequently, microlensing events are very rare–thus sparse in both time and space. These, hence, form an excellent evaluation platform for the development and application of CS. The mathematical technique implemented for CS exploits this sparsity inherent in gravitational microlensing and encodes the image during acquisition, significantly reducing data volume and for space flight instruments, it reduces onboard resources.[3,4] Similar to traditional methods, we apply data acquisition of the spatial images, followed by differencing to obtain a light curve representing a microlensing star over time. The differencing provides the relative change in pixel magnitude over time, as shown in Fig. 1.

Figure 2 shows the placement of a CS detector in a high-level block diagram.

In our previous work,[3–5] we did a preliminary analysis on the effects of CS on transient photometric measurements. In this work, we specifically analyze single and binary microlensing events and the implications of CS reconstruction on gravitational microlensing parameters of interest.

*Address all correspondence to Asmita Korde-Patel, asmita.a.korde@nasa.gov

2329-4124/2022/$28.00 © 2022 SPIE

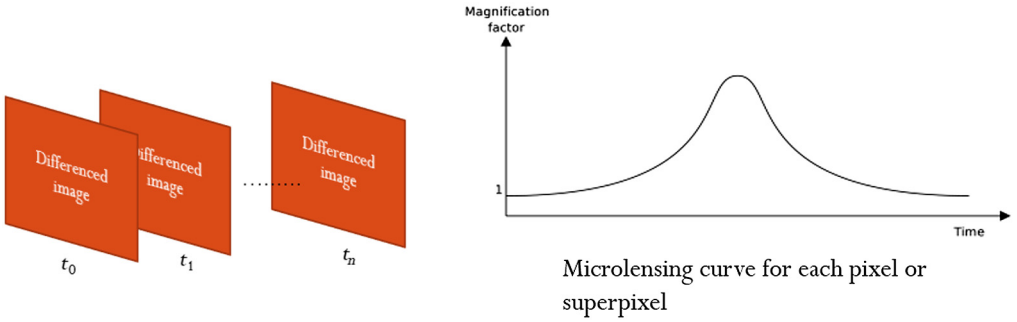

Fig. 1 Image differencing to generate a light curve over time, representing the change in magnification of a microlensing star.

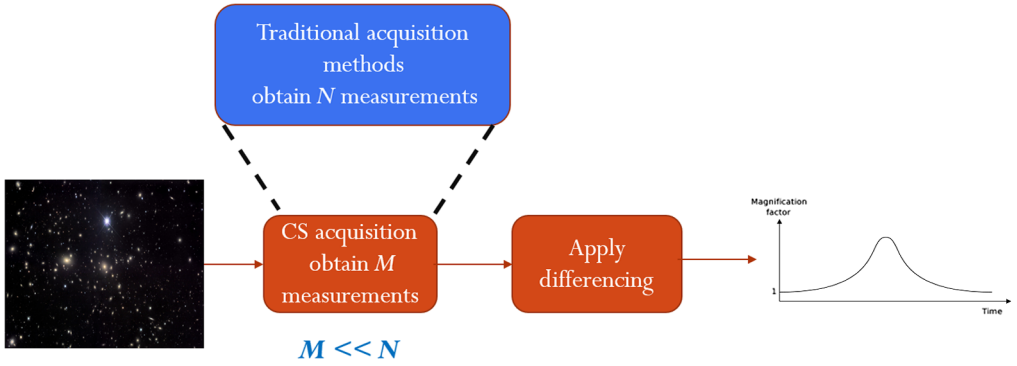

Fig. 2 CS detector will replace a traditional detector to acquire spatial images. The data acquired from the detector will be used to generate photometric light curves for microlensing events.

1.1 *Compressive Sensing*

CS is a mathematical theory for sampling at a rate much lower than the Nyquist rate, and yet, reconstructing the signal back with little or no loss of information. The signal is reconstructed by solving an underdetermined system. Sparsity in data sets is a key component required for the accuracy in reconstruction using CS methods. If it is not sparse in the sampling domain, we can transform it to a sparse domain, perform the reconstruction, and then transform it back to the original domain.[6,7] In a CS architecture, to acquire a signal of size n, we collect m measurements, where $m \ll n$. One measurement sample consists of a collective sum. We solve Eq. (1) to determine x through the observation y[8–12]

$$y_{m\times 1} = A_{m\times n} x_{n\times 1}. \tag{1}$$

Using the acquired measurements vector y and the known measurement matrix A, we can solve for a sparse x by applying various techniques, including greedy and optimization algorithms. Various reconstruction algorithms are discussed in the work of Pope.[13]

1.2 *Gravitational Microlensed Events*

In gravitational lensing, the surface brightness, which is the flux per area, is conserved. The total flux increases or decreases as the area increases or decreases. In microlensing, distinct images, due to the gravitational effects of the lensing system, are not seen, but rather, magnification or demagnification of the source star is observed; the images are not resolved. Since the Jacobian matrix gives the amount of change in the source star flux in each direction, the transformation of the original source to the "stretched" source, can be mapped by the Jacobian. The absolute value of the inverse of determinant gives the amount of magnification.

Einstein's ring forms when there is an exact alignment of the source, lens, and observer and is an important parameter for the basis of gravitational microlensing equations. Einstein's ring radius θ_E can be defined by Eq. (2), which is given as

$$\theta_E = \sqrt{\frac{4GMD_{LS}}{c^2 D_L D_S}}, \tag{2}$$

where M is the the mass of the lensing system, D_{LS} is the distance from the lens to the source, D_L is the distance from the observer to the lensing system, and D_S is the distance from the observer to the source.[1,14]

1.3 *Single Lens Gravitationally Microlensed Events*

Here, we describe the amplification value for each time as the source star moves in relation to the lensing system. Let u represent source position, and y represent image position, normalized by θ_E. Then, the lensing equation for a single-lens microlensing event can be given as Eq. (3),[1] which is given by

$$y_{\pm} = \pm\frac{\sqrt{u^2+4} \pm u}{2}. \tag{3}$$

Total amplification of the two images formed is given by

$$A(u) = \frac{u^2+2}{u\sqrt{u^2+4}}. \tag{4}$$

Due to the relative motion between the lens and source, amplification is dependent on the position of the source image at each time, t. Equation (5) shows the position of the source at each time given the trajectory the source takes[1]

$$u(t) = \left[u_0^2 + \left(\frac{t-t_0}{t_E}\right)^2\right]^{1/2}. \tag{5}$$

The trajectory is defined by the impact parameter, u_0, which is the minimum apparent separation between the lens and source in units of θ_E. Einstein ring radius crossing time is given by t_E and the time of peak magnification is given by t_0.[1] The amplification with time dependency is shown in Eq. (6)

$$A(t) = \frac{u_0^2 + \left(\frac{t-t_0}{t_E}\right)^2 + 2}{\left[u_0^2 + \left(\frac{t-t_0 2}{t_E}\right)\right]^{1/2}\left[u_0^2 + \left(\frac{t-t_0}{t_E}\right)^2 + 4)\right]^{1/2}}. \tag{6}$$

1.4 *Error Sensitivity*

In this section, we show the relation of the error to the sensitivity of the parameter θ_E. For an error of $\epsilon(t)$ in the change in amplification at any given time, the amplification at each time changes by $A(t) + \epsilon(t)$. This change in $\epsilon(t)$ at each time, t, changes the amplification equation derived due to two images resulting from a single-lens microlensing event. Using Eqs. (5) and (6), Eq. (7) can be written as

$$A(t) = \frac{u^2(t)+2}{u(t)\sqrt{[u^2(t)+4]}}. \tag{7}$$

Incorporating error, we get Eq. (8), which is stated as follows:

$$A(t)+\epsilon(t)=\frac{u^2(t)+2+\epsilon(t)\left[u(t)\sqrt{u^2(t)+4}\right]}{u(t)\sqrt{u^2(t)+4}}. \tag{8}$$

From Eq. (8), it is evident that a change in the light curve due to an error, $\epsilon(t)$, will not merely result in a change in u_0, but rather a change in the lensing system itself. That is, the light curve produced would not be accurately mapped to a lensing system.

In order to better understand the analytical effects of error on science parameters, here, we show the effect of the change in science parameters and the implications for the amplification value. For a change of γ in the value of θ_E, which depends on the properties of the lensing system, as noted in Eq. (2), we can define, $\tilde{\theta}_E$ as

$$\tilde{\theta}_E=\gamma\theta_E. \tag{9}$$

Using this $\tilde{\theta}_E$ in the lensing system, we derive the new amplification curve shown in Eq. (11). In our model, for $\tilde{A}(t)$, we scale u_0 by θ_E and not by $\tilde{\theta}_E$ to keep the same u_0 scale for comparison to $A(t)$

$$A(u)=\frac{u^2+2\gamma^2}{u\sqrt{u^2+4\gamma^2}}. \tag{10}$$

Expanding to include the definition of $u(t)$, we get Eq. (11)

$$\tilde{A}(t)=\frac{u_0^2+\left(\frac{t-t_0}{t_E}\right)^2+2\gamma^2}{\left[u_0^2+\left(\frac{t-t_0}{t_E}\right)^2\right]^{1/2}\left[u_0^2+\left(\frac{t-t_0}{t_E}\right)^2+4\gamma^2)\right]^{1/2}}. \tag{11}$$

To analyze the effect of CS errors, for single microlensing events, we consider the effect of θ_E on the amplification value. In Eq. (6), u_0 is in units of θ_E. Hence, a change of γ in θ_E, will directly affect the mass and distance parameters, M, D_LS, D_L, and D_S of the lensing system. Our CS-based modeling incorporates γ to determine the effect of errors due to CS application on the value of θ_E.

For astronomical measurements, the detector measures the flux of the source star. Hence, for microlensing, the total flux received from the source star is given by Eq. (12)

$$F(t)=F_sA(t)+F_b, \tag{12}$$

where F_s is the flux from the source, A is the amplification amount, and F_b is the blended flux. In our simulation modeling, we use $F_b=0$ for simplicity.

1.5 *Binary-Lensed Gravitational Microlensed Events*

A binary microlensed system consists of two lensing bodies, which act as a lens, deflecting the light from the observed source star. Here, we have two lensing bodies with mass, m_1 and m_2, where $m_1+m_2=M$. The source position is given by $\overline{\Psi}$. The image positions are given by Eq. (13)[1]

$$\overline{z}=\overline{\Psi}+\frac{m_1}{z-z_1}+\frac{m_2}{z-z_2}. \tag{13}$$

The amplification due to this lensing system is given by the ratio of the total area of the images to the total area of the source. Finding the amplification at each time is given by the following process:[15]

1. Find the roots of the polynomial given by the lensing Eq. (13).
2. Determine the boundaries of the images given the critical curves. The Jacobian of the lensing equation is used to determine the boundaries.

3. Find the area of all the images bounded by the critical curves.
4. Total amplification is given by Eq. (14)

$$A = \frac{A_I}{A_S}, \tag{14}$$

where A is the amplification value, A_I is the total area of all the images produced due to lensing, and A_S is the area of source star.

For an error, ϵ, in the amplification, that is, $\tilde{A} = A \pm \epsilon$ we can say either $\tilde{A}_I = A_I \pm \delta_1$ or $\tilde{A}_S = A_S \pm \delta_2$. The area of the source star is determined by the source star radius, ρ, mass ratio, q, and the separation between the two lenses, s. Amplification as a function of time is dependent on the trajectory angle, α. The solution to this fifth-order polynomial contains either three or five formed images. To determine the total area of the three or five images, Green's theorem is used.[15] The magnification is given by the relative motion of the source star and lensing system.

In this work, we examine single- and binary-lens caustics. A single-lens event will have a caustic as a point. Hence the observed light curve should have a single peak as it approaches the caustic. Binary-lens caustics are more complicated and can be characterized by three different categories namely close, intermediate, and wide. The three categories are divided based on the combination of the mass ratio and the separation between the two lensing masses.[1] Binary sources, as well as binary lenses could cause two peaks as depicted in our simulated light curves (Sec. 3). However, when generating light curves, we focus on the magnification due to binary lensing. Thus, a generalization of our CS results would be applicable for binary sources as well. Caustic curves represent closed loci where the magnification of a point source goes to infinity. Change in magnification as a function of time, depends on

1. ρ: source star radius,
2. α: trajectory angle,
3. q: ratio of the mass of the two lensing bodies,
4. s: distance between the two lensing bodies.

For a given q value, the topography changes to one, two, or three caustic curves based on the value of s. In terms of the magnification curve, the change in the number of caustics can result in different light curve signatures as the source crosses the caustic.

Mass ratio, q, and separation parameter, s, have a direct effect on the caustic topography generated. In this work, we focus on the error caused due to small changes, δ and ϵ, in q and s, respectively.

We show the error sensitivity for $\delta = 0.1q$ and $\epsilon = 0.1s$. In order to study error sensitivity, we choose points on the topography map in Ref. 14 well within each region, so that the change in the parameter does not result in a change in caustic topography.

For all our simulation analysis, we use the sensitivity of 10%, hence $q \pm 0.1q$ and $s \pm 0.1s$.

2 Compressive Sensing Simulations Setup

Microlensing is typically detected in crowded stellar fields. Although the spatial images are densely populated, the microlensed events are very rare, hence, only stars with a transient magnification are of interest to astronomers. In order to eliminate constant star sources in crowded fields, differencing can be applied. Through our previous work,[5] we show that CS can be applied on crowded star fields to produce differenced images, preserving the microlensed star magnification, with a very low error when the point spread function (PSF) of the two differenced images are the same.

2.1 *Compressive Sensing Architecture and Process*

In our simulations, we use CS framework based on our previous work.[5] An architectural diagram is shown in Fig. 3.

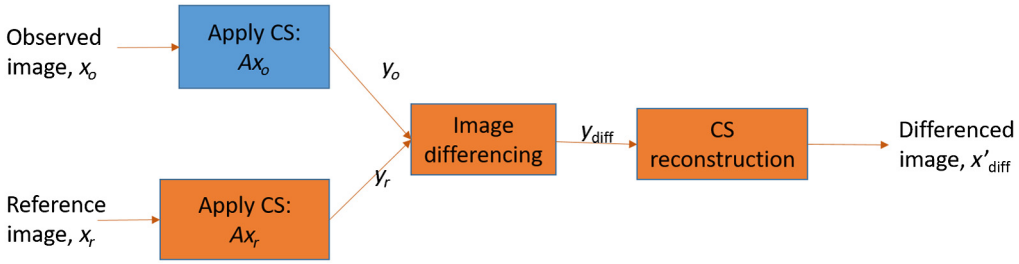

Fig. 3 CS architecture used for obtaining differenced images with star sources varying in flux due to a gravitational microlensing event.

In this work, we define a reference image, x_r, as an image of a spatial region, x, with a PSF, P_r, while an observed image, x_o, is defined as an image of the same spatial region, x, but with a different PSF, P_o. A reference image has a narrower PSF, resulting in a cleaner image as compared to an observed image. The architecture is implemented in the following manner:

1. Obtain CS-based measurements, y_o, for a spatial image.

CS can be applied by projecting a matrix, A, onto the region of interest, x_o. This can be done on a column-by-column basis for an $n \times n$ spatial region, x_o. Thus, for two-dimensional (2D) images, y_0 and A are of size $m \times n$, where $m \ll n$.

2. Given A and a clean reference image, x_r, construct measurements matrix y_r, where $y_r = Ax_r$.
3. Apply a 2D differencing algorithm on y_o and y_r to obtain a differenced image, y_{diff}, and the corresponding convolution kernel, M, which is used to match the observed and reference CS measurement vectors, y_o and y_r.[16] In our modeling, we use $y_{\text{diff}} = y_o - y_r$, by using the assumption that the PSF of the reference and observed image is the same as discussed in Sec. 2.2.
4. Reconstruct the differenced image, x'_{diff} using CS reconstruction algorithms, given A and y_{diff}.

2.2 *Assumptions in Our Model*

To understand merely the effects of CS on photometric measurements, we eliminate the following variables in our simulations. In future work, we will incorporate each of these factors one at a time to thoroughly understand the effect of each one in our CS-based framework. The two assumptions we make are:

1. The PSF of the reference image and the observed image is the same. This would typically be the case for space-borne observatories in which the PSF changes very slowly, if at all. The two images differ in any magnification of a star source due to a transient event.

   In applications where the PSF of the reference and observed images are different, Eq. (16) is used

$$y_{\text{diff}} = Ax_o - (Ax_r \star M), \tag{15}$$

$$= y_o - (y_r \star M). \tag{16}$$

   where the star symbol represents convolution. However, in our models, for simplicity, we assume the same PSF for a reference and observed image, thus resulting in Eq. (19)

$$y_{\text{diff}} = A(x_{\text{diff}}), \tag{17}$$

$$= A(x_o) - A(x_r), \tag{18}$$

$$= y_o - y_r. \tag{19}$$

Hence, in Fig. 3, image differencing consists of subtracting the reference measurements from the observed measurements. In non-ideal cases, when the PSF of the reference image is different as compared to the observed image, image differencing algorithms can be added. However, that adds another layer of uncertainty and error, which we needed to eliminate for our purpose of understanding purely the effects of CS acquisition and reconstruction.

2. There is no noise present.

   To eliminate added complexity in this preliminary study, we do not incorporate any noise. In future studies, we will add detector noise, measurement noise, as well as any background noise.

   For a practical approach, we can assume the effects of noise to be minimal if the signal-to-noise ratio (SNR) during a magnification event for the specific group of pixels representing the microlensing star is sufficiently high, such that, the sparsity content of the image is preserved. In Sec. 3, we briefly show the basic effect of CS reconstruction for degrading SNR for an image with Gaussian added noise.

2.3 *Simulation Setup Parameters*

In our simulations, we use a 128×128 size image. In order to depict a crowded stellar field, we generate the number of star sources to be 75% of the total number of pixels. To simulate realistic fields, we use airy shaped PSFs with varying radius and fluxes of the star sources. The radius ranges from [0, 5] pixel units and flux ranges from [50, 5000] pixel counts. We perform 100 Monte Carlo simulations for each set of parameter values discussed later in this section. For each of the 100 Monte Carlo simulations, the crowded stellar field is changed, including the PSF radius and flux values of each star source generated. In addition, for each simulation, the Bernoulli random values in A are changed. We use orthogonal matching pursuit algorithm, as provided by Python libraries, for reconstruction.

2.3.1 *Compressive sensing parameters*

For an $n \times n$ size spatial image, we use a measurement matrix, A, of size $m \times n$ to obtain the measurements, y, of size $m \times n$. Hence, our compression factor is $\frac{m}{n}$.

For both single-lens and binary-lens event simulations, we use the following CS parameters.

- Number of measurements, $m = 25\%$ of n.
- Measurement matrix, A, consists of Bernoulli random variables of values 1 and 0. These values were chosen such that the matrix can be relevant for practical application.

2.3.2 *Gravitational microlensing parameters*

We simulate microlensing events for single-lens and binary-lens systems.

Single microlensing events. For each of the simulation cases, u_0 and t_0 are varied in the simulation setup. The other parameters from Eq. (6) are shown in Table 1.

Table 1 Single microlensing event equation parameters used for CS simulation modeling.

Parameter	Value
u_0	0.01, 0.1, 0.5
t_0	13, 15, 17
t_e	30

Table 2 Binary microlensing event equation parameters used for CS simulation modeling.

Parameter	Close	Intermediate	Wide
s	0.6	1	1.7
q	1	0.1	0.01
ρ	0.01	0.01	0.01
α	0.03	0.93	0.03
t_E	100.3	100.3	100.3
t_0	7154	7154	7154
u_0	0.1	0.2	0.3

Binary microlensing events. For binary microlensing events, we perform simulations for each of the three topographies with the parameters described in Table 2 are stated as follows:

1. s: separation between the two masses in the lensing system in units of total angular Einstein radii,
2. q: mass ratio of the two lenses,
3. ρ: source radius in units of Einstein's ring radius,
4. α: trajectory angle between lens axis and source,
5. t_E: Einstein ring radius crossing time,
6. t_0: time of peak magnification,
7. u_0: impact parameter in units of Einstein's ring radius.

2.3.3 *Error calculations*

We calculate the % error based on the total flux of the microlensing star in a three-pixel unit radius from the center pixel of the star. Error is calculated using

$$\frac{|f'_{\text{diff}} - f_{\text{diff}}|}{f_{\text{diff}}} \times 100\%, \tag{20}$$

where f'_{diff} and f_{diff} are the total fluxes within the three-pixel radius of the source positions of the reconstructed and original differenced images, respectively.

3 Simulation Results

3.1 *Single-Lens Events*

In this first set of simulations, we vary u_0, while keeping $t_0 = 15$ and $t_e = 30$ constant.

Amplifications for single-lens microlensing events are generated using Eq. (6). We compare the CS reconstruction with error due to a γ change in θ_E as described in Eq. (11), where $\gamma = 1 \pm 0.1$. Hence $\theta_E = 0.9\theta_E$ and $\theta_E = 1.1\theta_E$.

In Figs. 4–9, we show the simulations for u_0 = 0.01, 0.1, and 0.5. In the next set of simulations, as shown in Figs. 10–13, we use $u_0 = 0.1$ and vary t_0 with $t_0 = 13$ and $t_0 = 17$.

Tables 3–7 show the error values for each of the corresponding set of parameters used for the simulations. Our simulations show that CS reconstruction is affected by the magnification value of the source star in each differenced image. For low magnification events, such as the one caused by $u_0 = 0.5$, the error in CS reconstruction is higher. The results in Ref. 5 also indicate that CS reconstruction accuracy is dependent on the magnification of the event, which in turn

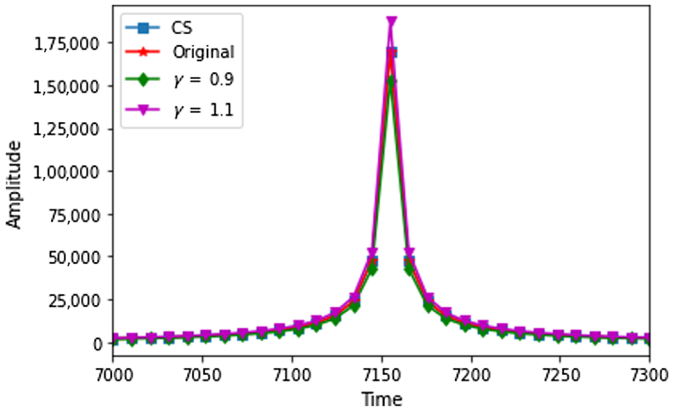

Fig. 4 Single-lens microlensing event, $u_0 = 0.01$. The original simulated microlensing curve along with the CS reconstruction and the microlensing curve generated due to a change γ in θ_E is shown.

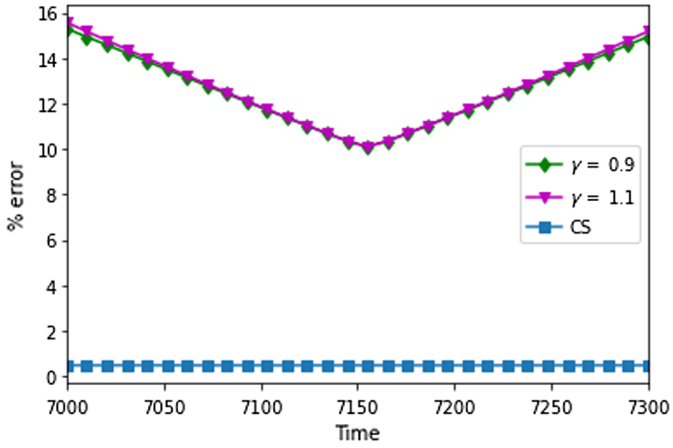

Fig. 5 Percent errors for the single-lens event, $u_0 = 0.01$ for CS reconstruction and the change in microlensing light curve generated due to γ changes in θ_E as compared to the original simulated microlensing curve for the light curves in Fig. 4.

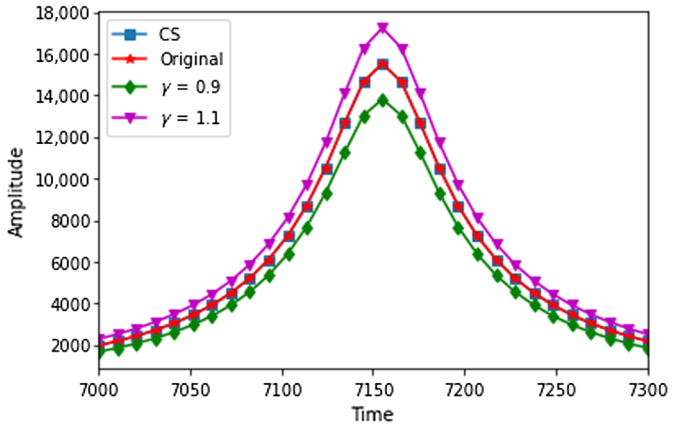

Fig. 6 Single-lens microlensing event, $u_0 = 0.1$. The original simulated microlensing curve along with the CS reconstruction and the microlensing curve generated due to a change in γ in θ_E is shown.

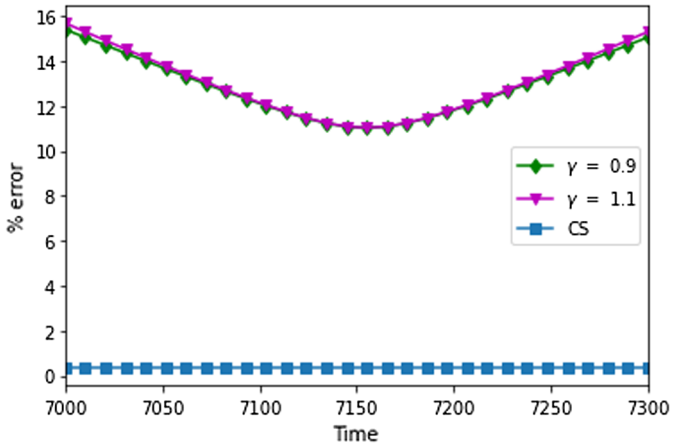

Fig. 7 Percent errors for the single-lens event, $u_0 = 0.1$ for CS reconstruction and the change in microlensing light curve generated due to γ changes in θ_E as compared to the original simulated microlensing curve for the light curves in Fig. 6.

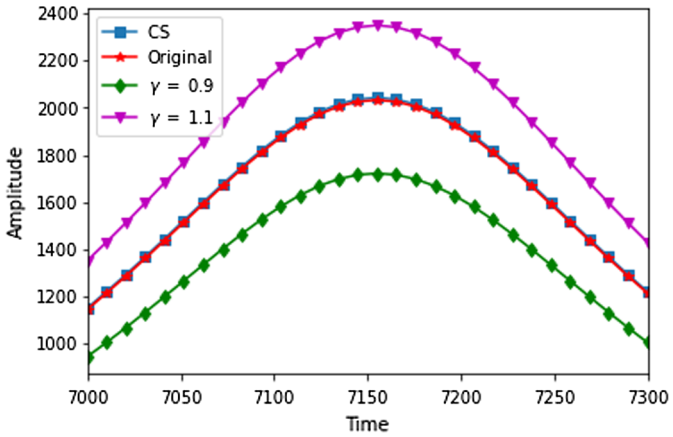

Fig. 8 Single-lens microlensing event, $u_0 = 0.5$. The original simulated microlensing curve along with the CS reconstruction and the microlensing curve generated due to a change in γ in θ_E is shown.

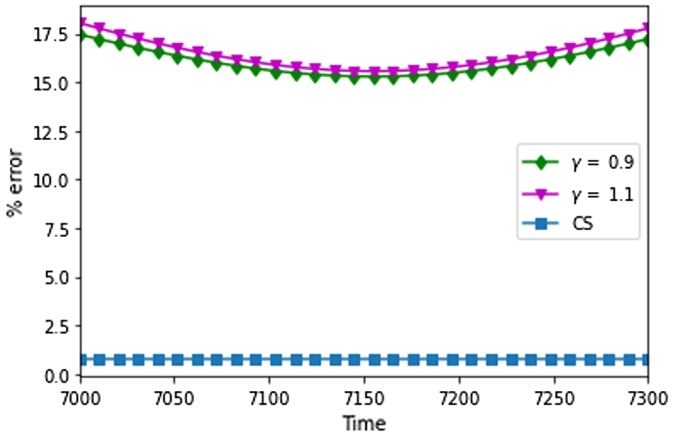

Fig. 9 Percent errors for the single-lens event, $u_0 = 0.5$ for CS reconstruction and the change in microlensing light curve generated due to γ changes in θ_E as compared to the original simulated microlensing curve for the light curves in Fig. 8.

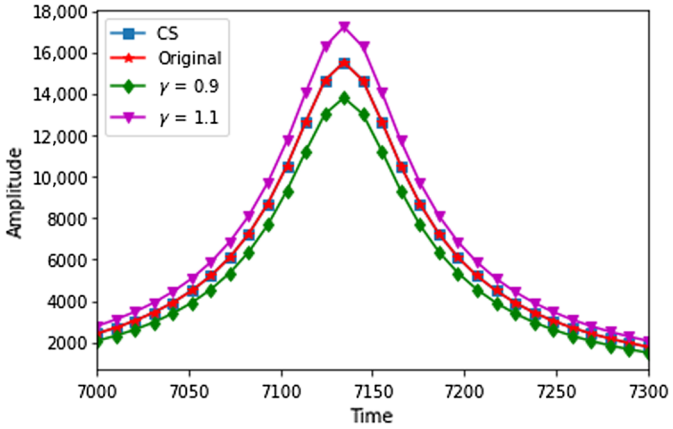

Fig. 10 Single-lens microlensing event, $t_0 = 13$. The original simulated microlensing curve along with the CS reconstruction and the microlensing curve generated due to a change in γ in θ_E is shown.

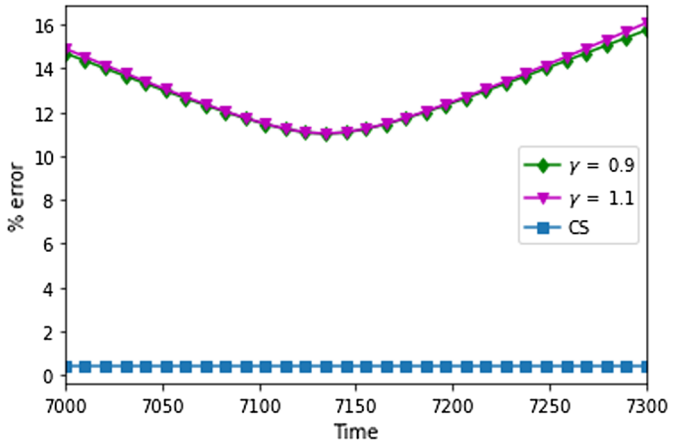

Fig. 11 Percent errors for single-lens event, $t_0 = 13$ for CS reconstruction and the change in microlensing light curve generated due to γ changes in θ_E as compared to the original simulated microlensing curve for the light curves in Fig. 10.

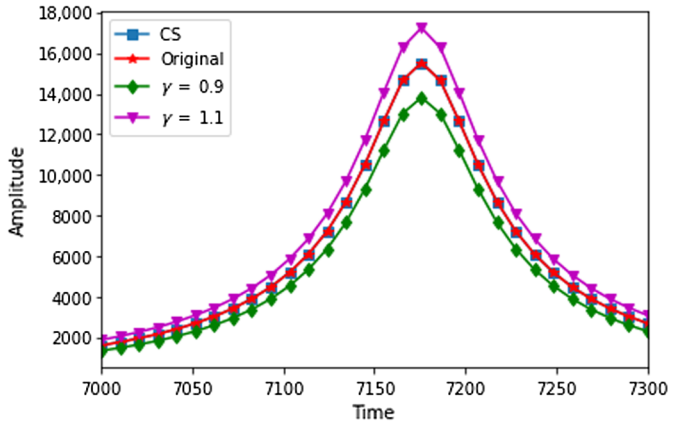

Fig. 12 Single-lens microlensing event, $t_0 = 17$. The original simulated microlensing curve along with the CS reconstruction and the microlensing curve generated due to a change in γ in θ_E is shown.

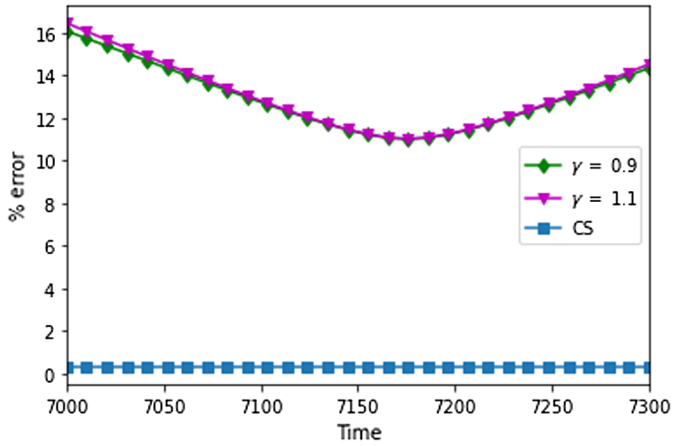

Fig. 13 Percent errors for single-lens event, $t_0 = 17$ for CS reconstruction and the change in microlensing light curve generated due to γ changes in θ_E as compared to the original simulated microlensing curve for the light curves in Fig. 12.

Table 3 Errors for single microlensing light curve with $u_0 = 0.01$.

Single-lens event with $u_0 = 0.01$	Average % error	Average standard deviation
CS	0.49	0.00
$\gamma = 0.9$	12.62	1.53
$\gamma = 1.1$	12.71	1.61

Table 4 Errors for single microlensing light curve with $u_0 = 0.1$.

Single-lens event with $u_0 = 0.1$	Average % error	Average standard deviation
CS	0.36	0.00
$\gamma = 0.9$	12.91	1.36
$\gamma = 1.1$	13.01	1.43

Table 5 Errors for single microlensing light curve with $u_0 = 0.5$.

Single-lens event with $u_0 = 0.5$	Average % error	Average standard deviation
CS	0.77	0.00
$\gamma = 0.9$	16.07	0.66
$\gamma = 1.1$	16.45	0.76

affects the sparsity of the data set. For a low magnification star in a differenced image, the rate of decay of the coefficients in the differenced images also decreases, hence, causing a higher error in CS reconstruction. The small fluctuations in the average error are due to the variation in Bernoulli random measurement matrix. From the error plots (7, 9, 5), we see that CS error is fairly constant, with little variability, over the microlensing curves for all u_0 and t_0 values.

Table 6 Errors for single microlensing light curve with $t_0 = 13$.

Single-lens event with $t_0 = 13$	Average % error	Average standard deviation
CS	0.42	0.00
$\gamma = 0.9$	12.94	1.40
$\gamma = 1.1$	13.03	1.48

Table 7 Errors for single microlensing light curve with $t_0 = 17$.

Single-lens event with $t_0 = 17$	Average % error	Average standard deviation
CS	0.32	0.00
$\gamma = 0.9$	12.98	1.48
$\gamma = 1.1$	13.09	1.57

3.1.1 *Error sensitivity of microlensing parameters*

In this section, we fit the differenced magnification curve and the CS reconstructed curve to obtain the microlensing parameters: F_s, F_b, t_0, t_E, and u_0. The differenced magnification curve is obtained from x_{diff} at the microlensing star source center pixel, $[p_x, p_y]$ and CS reconstructed magnification curve is obtained from $x'_{\text{diff}}[p_x, p_y]$. We use the same setup as in Sec. 2.3. We obtain the parameters for each CS reconstructed data set over the 100 Monte Carlo simulations and present the average derived value in Table 8. We used Mulens Model software for obtaining the parameters.[17] When we generated our magnification light curves, we used $F_b = 0$. However, due to the observed and reference image differencing, and the Mulens Model software modeling factors, we obtain a non-zero F_b during parameter fitting. Thus, in order to accurately understand the effect of CS reconstruction on the derivation of the parameters, we compare the Mulens Model software-derived parameters for $x_{\text{diff}}[p_x, p_y]$ with $x'_{\text{diff}}[p_x, p_y]$. The obtained results of the parameters depend on the initial guess provided. Hence, in our analysis, we vary the initial guess to determine the effects of CS, despite the initial guess values. Our true values are listed as follows:

- $t_0 = 15$,
- $t_E = 30$,
- $u_0 = 0.5$.

We use the initial values as shown in Table 9.

For each trial, we show the % error in the parameters derived from Mulens Model software between $x_{\text{diff}}[p_x, p_y]$ and $x'_{\text{diff}}[p_x, p_y]$ in Table 8.

Table 8 Derived parameter % errors.

Trial number	F_s	F_b	t_0	t_E	u_0
1	0.585	0.585	0.00	0.025	0.029
2	0.585	0.585	0.00	0.025	0.029
3	0.586	0.586	0.00	0.025	0.029
4	0.585	0.585	0.00	0.025	0.029

Table 9 Microlensing parameters used as initial guess for Mulens Model software.

Trial number	t_0	t_E	u_0
1	15	30	0.5
2	15	30	0.4
3	13	30	0.5
4	15	32	0.5

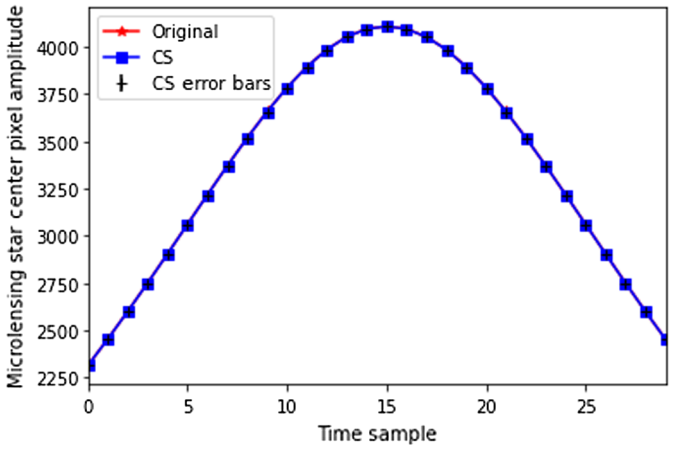

Fig. 14 Single-lens microlensing event CS reconstruction with error bars.

In all the different initialization parameters, there was a very insignificant difference in the % error for all of the parameters. The largest % error was in F_s and F_b. Hence, through this setup, we can say that F_s and F_b are most affected by CS reconstruction. In order to visually understand the effect of CS reconstruction on F_s, we simulate a star field and run CS reconstruction for 100 Monte Carlo simulations by varying the Bernoulli random matrix each time. Figure 14 shows the flux variation caused due to the CS measurement matrix, for a given star field with a source star experiencing a single-lens microlensing event with $\mu_0 = 0.5$. Similar to our other simulations, 25% CS measurements were used.

Figures 15 and 16 show detailed plots for some of the statistics for the data in Fig. 14.

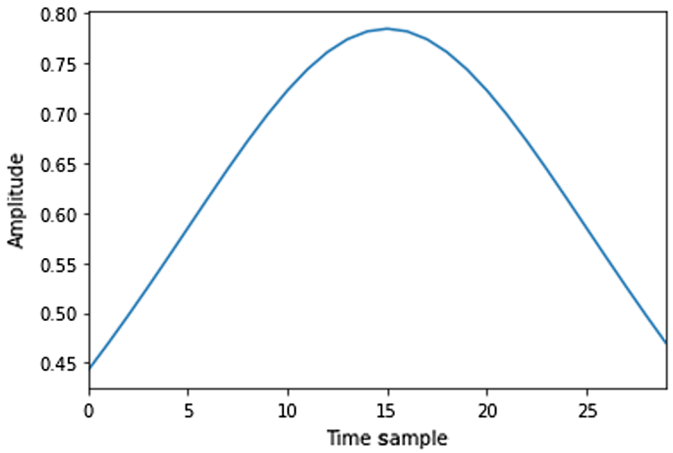

Fig. 15 Difference in amplitude between the original microlensing curve and average CS reconstruction microlensing curve for the data in Fig. 14.

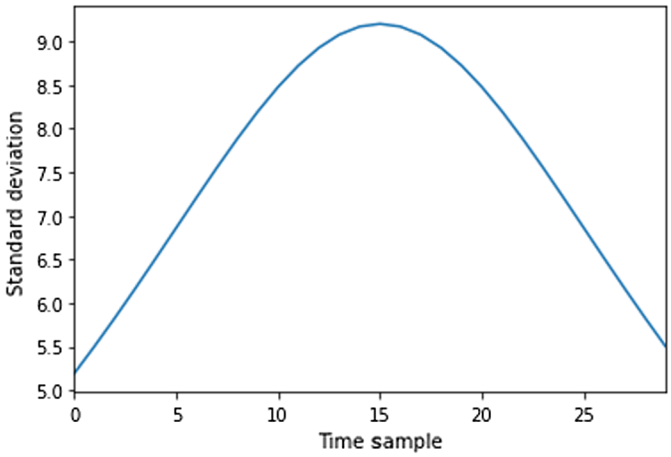

Fig. 16 Standard deviation of the CS reconstruction pixel values over 100 Monte Carlo simulations for each time sample for the data in Fig. 14.

For the data in Fig. 14, we explicitly show the standard deviation of the CS reconstruction curve over 100 Monte Carlo simulations for each time sample in Fig. 16.

As noted in Figs. 15 and 16, the variation in CS reconstruction, as calculated by the difference in pixel amplitude and the standard deviation, changes as a function of the pixel value of the original source star. That is, a smaller standard deviation is seen for time samples where the magnification is lower as compared to the time samples where the pixel magnification is higher.

3.1.2 *Noise effects on a single-lens microlensing event curve*

In this section, we briefly show the effect of Gaussian noise on the reconstruction of the microlensing event curves. From CS theory, it is known that the signal of interest is accurately reconstructed for sparse signals. Hence, adding noise to the spatial images can degrade the sparsity of the images. In our simulations, we add random Gaussian noise with mean = 0 and varying standard deviation to obtain images with different SNRs. CS architecture shown in Fig. 3 is applied, with the noise application on the observed image, x_o. In the noise simulation, 25% CS measurements were used. The error plot for the addition of Gaussian noise with different SNR values is shown in Fig. 17.

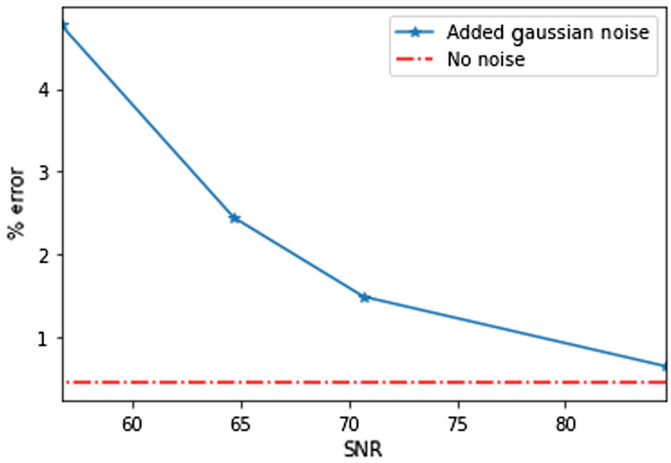

Fig. 17 Percent error as a function of image SNR. Images are generated by varying added Gaussian noise. The dashed red line represents the % error without any addition of noise.

From Fig. 17, it is evident that as SNR decreases, the % of error increases at a higher rate. The rate of increase is 0.06% error per SNR unit toward the higher SNR values and 0.29% error per SNR unit toward the lower SNR range.

3.2 *Binary-Lens Microlensing Events*

The amplification for the photometric curves is derived using gravitational microlensing equations, generated by the software provided in Ref. 15.

We perform simulations on the three categories as described in Sec. 1.5—close, intermediate, and wide. The parameters used for each of the simulations are shown in Table 10. Simulation results for each of the topography categories are shown in Figs. 18–26. Tables 11–13 list the error

Table 10 Values of s and q chosen for calculating error sensitivity, such that it is within 10% of the value chosen for the original caustic.

Caustic	Original s	$\pm 0.1s$	Original q	$\pm 0.1q$
Close	0.6	0.54, 0.66	1	0.9, 1.1
Intermediate	1	0.9, 1.1	0.1	0.09, 0.11
Wide	1.7	1.53, 1.87	0.01	0.009, 0.011

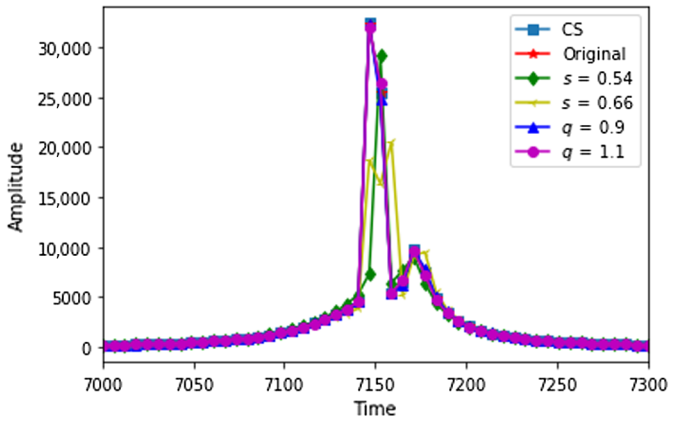

Fig. 18 Closed caustic microlensing curve with $s = 0.6$ and $q = 1$, shown along with the CS reconstruction, as well as the microlensing curve generated using $s = 0.54$, 0.66 and $q = 0.9$, 1.1.

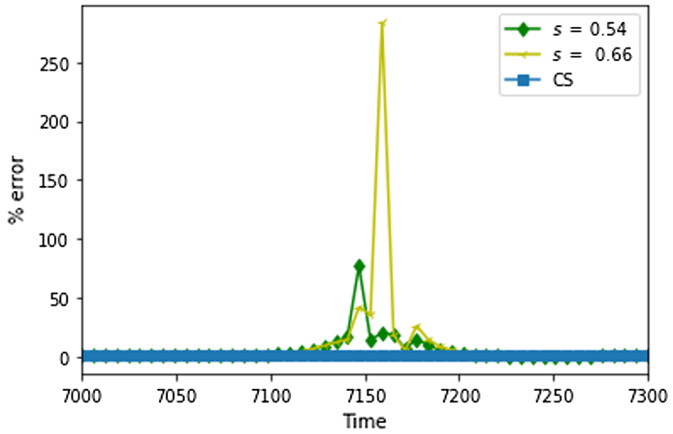

Fig. 19 % Error of CS reconstruction as compared to % error due to 10% deviation in the value of s.

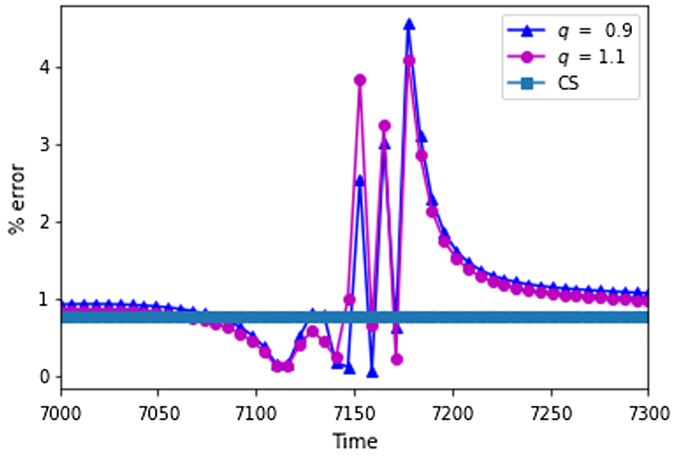

Fig. 20 % Error of CS reconstruction as compared to % error due to 10% deviation in the value of q.

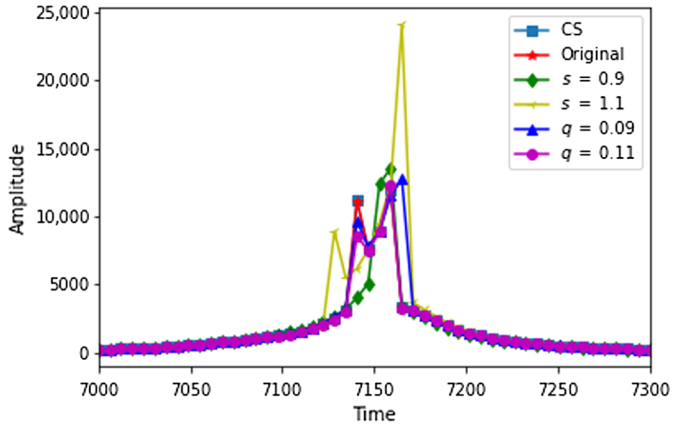

Fig. 21 Intermediate caustic microlensing curve with $s = 1$ and $q = 0.1$, shown along with the CS reconstruction, as well as the microlensing curve generated using $s = 0.9$, 1.1 and $q = 0.09$, 0.11.

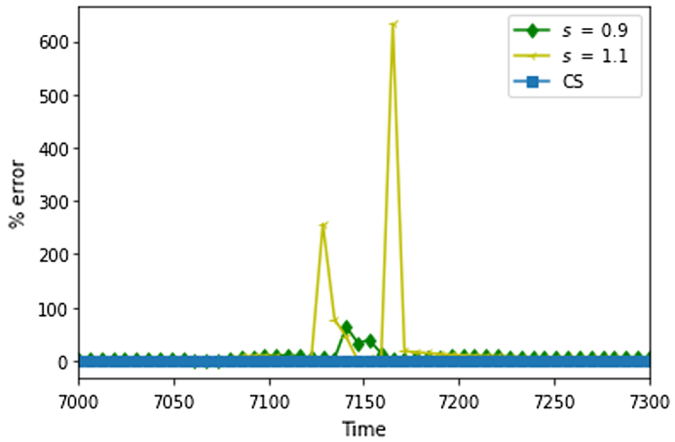

Fig. 22 % Error of CS reconstruction as compared to % error due to 10% deviation in the value of s for the given (Fig. 21) intermediate caustic binary-lensing light curve reconstruction.

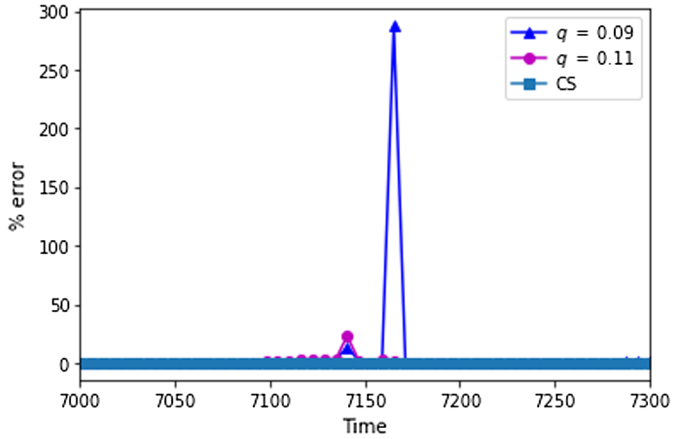

Fig. 23 % Error of CS reconstruction as compared to % error due to 10% deviation in the value of q for the given (Fig. 21) intermediate caustic binary-lensing light curve reconstruction.

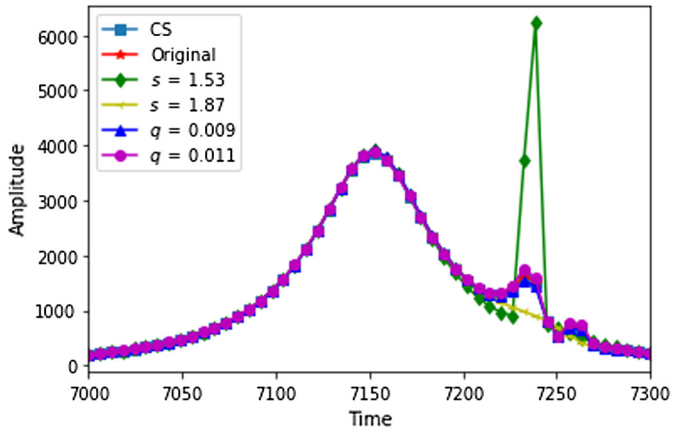

Fig. 24 Wide caustic microlensing curve with $s = 1.7$ and $q = 0.01$, shown along with the CS reconstruction, as well as the microlensing curve generated using $s = 1.53$, 1.87 and $q = 0.009$, 0.011.

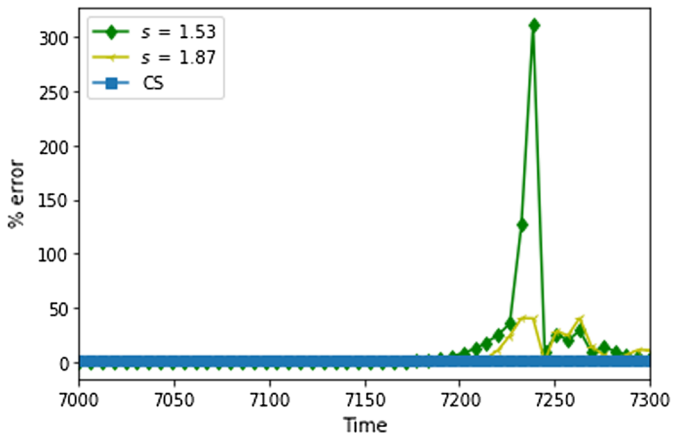

Fig. 25 % Error of CS reconstruction as compared to % error due to 10% deviation in the value of s for the given (Fig. 24) wide caustic binary-lensing light curve reconstruction.

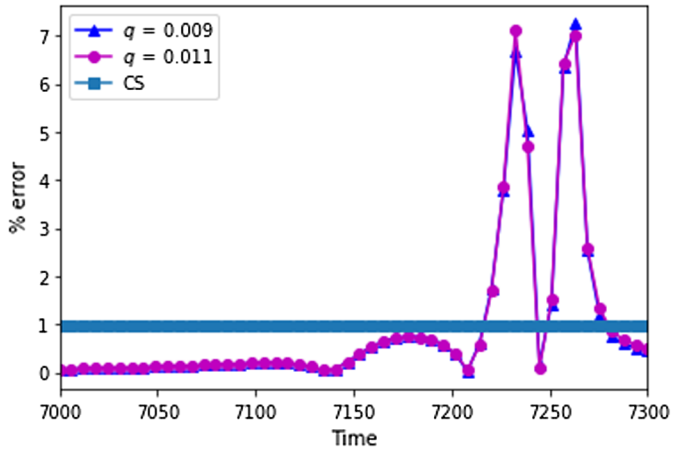

Fig. 26 Percent error of CS reconstruction as compared to % error due to 10% deviation in the value of q for the given (Fig. 24) wide caustic binary-lensing light curve reconstruction.

Table 11 Errors for close caustic topographies model for CS reconstruction, and for microlensing light curve generated due to 10% variation in s and q.

Close caustic	Average % error	Avg. standard deviation of the % error
CS	0.76	0.00
$s = 0.54$	0.52	11.52
$s = 0.66$	10.47	40.02
$q = 0.9$	1.11	0.80
$q = 1.1$	1.07	0.82

Table 12 Errors for intermediate caustic topographies model for CS reconstruction, and for microlensing light curve generated due to 10% variation in s and q.

Intermediate caustic	Average % error	Avg. standard deviation of the % error
CS	0.61	0.00
$s = 0.9$	7.74	10.45
$s = 1.1$	25.86	94.24
$q = 0.09$	6.76	40.14
$q = 0.11$	1.13	3.23

values for each of the categories. To determine error sensitivity in terms of impact on the separation parameter, s, and mass ratio, q, we compare the CS reconstruction with the following values of s and q, thereby providing CS reconstruction accuracy bounds of 10% for the value of s and q.

Our simulations show that we can attain error less than 1% using 25% of the Nyquist rate measurements. In addition, the error obtained through CS reconstruction will be well within 10% deviation in verified microlensing parameters of θ_E, s, and q.

Table 13 Errors for wide caustic topographies model for CS reconstruction, and for microlensing light curve generated due to 10% variation in s and q.

Wide caustic	Average % error	Avg. standard deviation of the % error
CS	0.97	0.00
$s = 1.53$	13.64	46.57
$s = 1.87$	5.54	11.02
$q = 0.009$	0.96	1.73
$q = 0.011$	0.97	1.74

4 Conclusions and Future Work

Using this technique we provide limitations on the sensitivity of detection of planetary perturbations given our CS parameters. We show examples of the effects of error tolerance on the science parameters that are of importance in the microlensing curves. For both single and binary microlensed events, we provide examples of the changes in the microlensing parameters due to minimal error tolerance. This gives a bound for analyzing the effects of CS for the application of gravitational microlensing. These are simulated theoretical error bounds for given sensitivities—the sensitivity of the detectors and technology currently used may not be sensitive to such δ changes in the science parameters. For single-lensed microlesning events, we showed the CS reconstruction error as compared to error from $\pm 10\%$ in θ_E. Our results show that CS is sensitive to changes in u_0 and not to changes in t_0, as t_0 causes merely a shift in data, while u_0 causes a change in magnification value. Through our analysis for microlensing parameter fitting, we show that CS is most sensitive to F_s and F_b. For binary-lensed microlensing events, we show CS reconstruction error to be within $\pm 10\%$ of the mass ratio and the separation between the two lenses. Our work shows that we can reconstruct microlensing light curves using 25% of the required Nyquist rate measurements with an error <1%. In terms of microlensing sensitivity, we show that this error is within the bounds of 10% θ_E for single microlensed events and within 10% of q and s for binary microlensed events. In this work, we only focus on bounds determined by our simulated models using microlensing theory and disregard detector optics effects. In cases where less sensitivity is affordable, fewer measurements can be used to further save onboard resources. Conversely, if more sensitivity to perturbations is required the number of measurements can be increased. This technique works with high accuracy, with less than 1% error for crowded stellar fields with the same PSFs for a reference and observed image.

Our future work will incorporate noise analysis, as well as the implementation of this CS architecture for reference and observed images with different PSFs. In the case of different PSFs, we will understand the efficacy of differencing algorithms used in astronomical applications.

Acknowledgments

There are no conflicts of interest.

References

1. S. Seager, *Exoplanets*, University of Arizona Press (2010).
2. D. P. Bennett and S. H. Rhie, "Simulation of a space-based microlensing survey for terrestrial extrasolar planets," *Astrophys. J.* **574**(2), 985 (2002).
3. A. Korde-Patel, R. K. Barry, and T. Mohsenin, "Application of compressive sensing to gravitational microlensing experiments," *Proc. Int. Astron. Union* **12**(S325), 67–70 (2016).

4. A. Korde-Patel, R. K. Barry, and T. Mohsenin, "Application of compressive sensing to gravitational microlensing data and implications for miniaturized space observatories" (2016).
5. A. Korde-Patel, R. K. Barry, and T. Mohsenin, "Compressive sensing based data acquisition architecture for transient stellar events in crowded star fields," in *IEEE Int. Instrum. and Meas. Technol. Conf.*, IEEE, (2020).
6. J.-L. Starck, F. Murtagh, and J. M. Fadili, *Sparse Image and Signal Processing: Wavelets, Curvelets, Morphological Diversity*, Cambridge University Press, New York (2010).
7. L. Rebollo-Neira and J. Bowley, "Sparse representation of astronomical images," *J. Opt. Soc. Am. A* **30**(4), 758–768 (2013).
8. Y. C. Eldar and G. Kutyniok, *Compressed Sensing: Theory and Applications*, Cambridge University Press, New York (2012).
9. E. J. Candès and M. B. Wakin, "An introduction to compressive sampling [a sensing/sampling paradigm that goes against the common knowledge in data acquisition]," *IEEE Signal Process Mag.* **25**(2), 21–30 (2008).
10. E. Candes and J. Romberg, "Sparsity and incoherence in compressive sampling," *Inverse Prob.* **23**(3), 969 (2007).
11. J. Bobin, J.-L. Starck, and R. Ottensamer, "Compressed sensing in astronomy," *IEEE J. Sel. Top. Signal Process.* **2**(5), 718–726 (2008).
12. M. B. Wakin et al., "An architecture for compressive imaging," in *Int. Conf. Image Process.*, IEEE (2006).
13. G. Pope, "Compressive sensing: a summary of reconstruction algorithms," in MS thesis ETH, Swiss Federal Institute of Technology Zurich, Department of Computer Science (2009).
14. Y. Tsapras, "Microlensing searches for exoplanets," *Geosciences* **8**(10), 365 (2018).
15. V. Bozza, "Microlensing with an advanced contour integration algorithm: Green's theorem to third order, error control, optimal sampling and limb darkening," *Mon. Not. R. Astron. Soc.* **408**(4), 2188–2200 (2010).
16. D. M. Bramich, "A new algorithm for difference image analysis," *Mon. Not. R. Astron. Soc. Lett.* **386**(1), L77–L81 (2008).
17. R. Poleski and J. C. Yee, "Modeling microlensing events with Mulens Model," *Astron. Comput.* **26**, 35–49 (2019).

Asmita Korde-Patel is a civil servant at NASA Goddard Space Flight Center in the Instrument Electronics Development branch. She works on implementing algorithms onto hardware for space flight instruments. She is currently pursuing her PhD in electrical engineering at University of Maryland, Baltimore County. Her research interest lies in applying compressive sensing (CS) to transient photometric measurements. Specifically, she is studying the effects of CS application for gravitational microlensing, a technique used to detect exoplanets.

Richard K. Barry is an astronomer in NASA's Laboratory for Exoplanets and Stellar Astrophysics. His principal research involves the detection and characterization of new exoplanets using the techniques of gravitational microlensing and transits. He also has worked as a NASA Space Shuttle engineer, power systems engineer, instrument design engineer, and USAF technician on F16 aircraft.

Tinoosh Mohsenin is an associate professor in the Department of Computer Science and Electrical Engineering at University of Maryland, Baltimore County. She received her PhD from the University of California, Davis in 2010. She has authored or co-authored more than 130 peer-reviewed journals and conference publications. Her research focus is on designing energy-efficient embedded processors for machine learning and signal processing, knowledge extraction techniques for autonomous systems, wearable smart health monitoring, and embedded big data computing.